Additive manufacturing of high-entropy alloys

Contents

Introduction

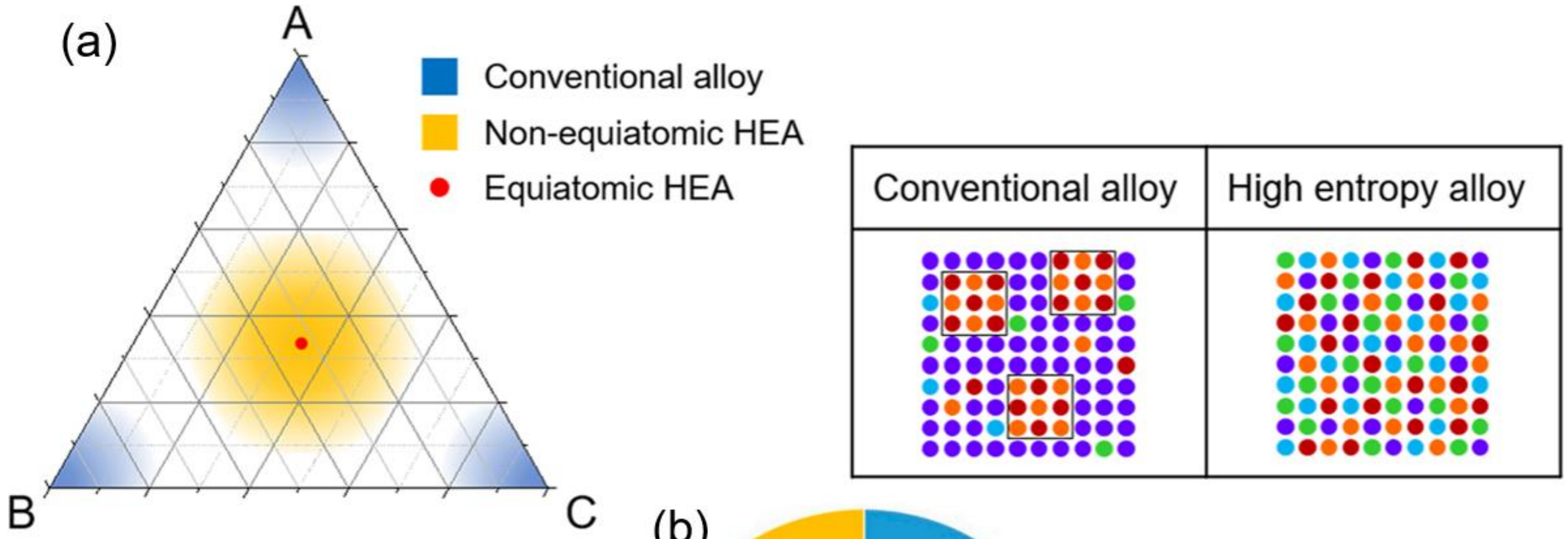

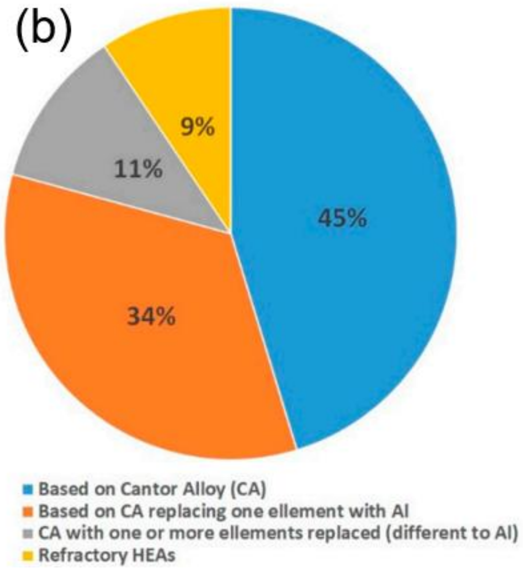

Fig. (a) The compositional range of conventional alloy (blue region), non-equiatomic HEA (yellow region), and equiatomic HEA (red region) in a schematic ternary phase diagram of multicomponent alloy systems, as well as an illustration of the atomic distribution of HEAs and common alloys (The boxed black line displays ordered intermetallic/intermediate compounds, and each coloured dot represents a different type of element, and (b) Quantitative classification of AMed HEAs

Source: [(a)] Source: Kim et al. 2020 [https://doi.org/10.1557/jmr.2020.140]
[(b)]Torralba, and Campos 2020 [https://doi.org/10.3390/met10050639]

Cantor alloy

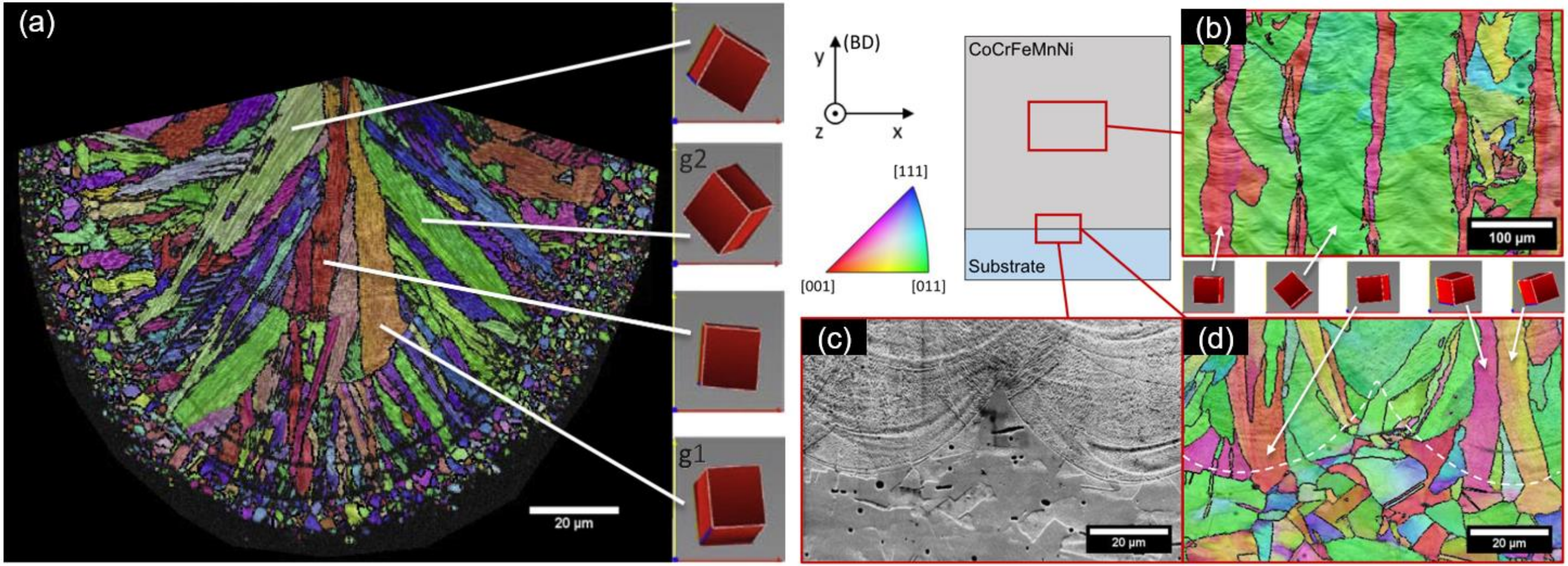

Fig. (a) EBSD IPF map of a cross section of a single-layer LPBFed CA, (b) EBSD IPF map of a LPBFed CA cubic build, (c) and (d) SEM micrograph and its relevant EBSD IPF map of the build/substrate interface of LPBFed CA

Source: Piglione et al. 2018 [https://doi.org/10.1016/j.matlet.2018.04.052]

Cantor alloy

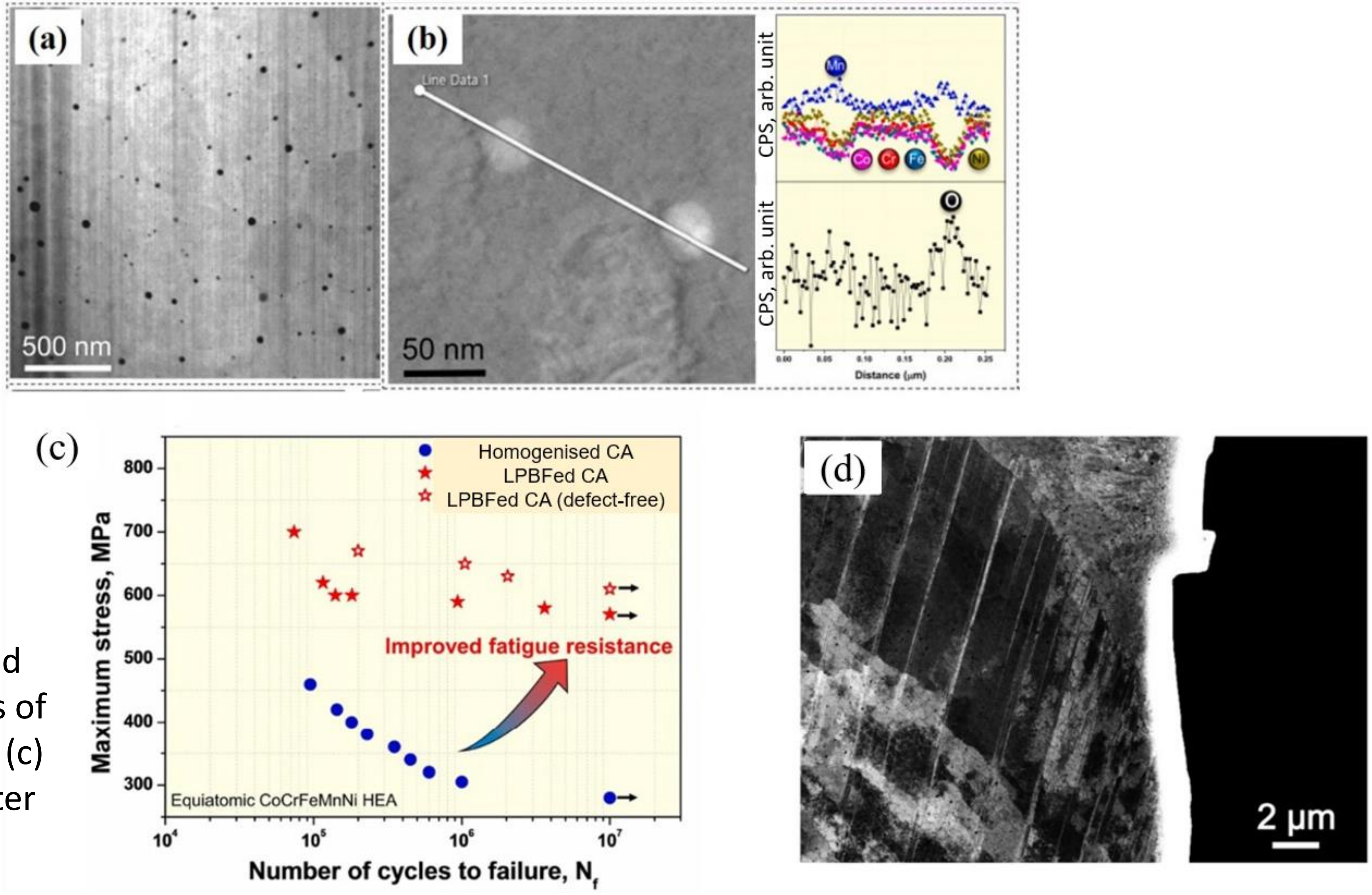

Fig. (a) Cellular walls with nanoprecipitates in LPBFed CA, (b) Establishing that nanoprecipitates are Mn_2O_3, based on EDS line analysis (Blue, purple, red, light blue, yellow, and black circles and signs denote elements of Mn, Co, Cr, Fe, Ni, and O, respectively), (c) CA fatigue life curves after LPBF and after conventional processing, and (d) After failure, a dense cluster of deformation twins formed at the specimen surface

Source: Guan et al. 2021 [https://doi.org/10.1007/s11669-021-00913-w]

Cantoralloy

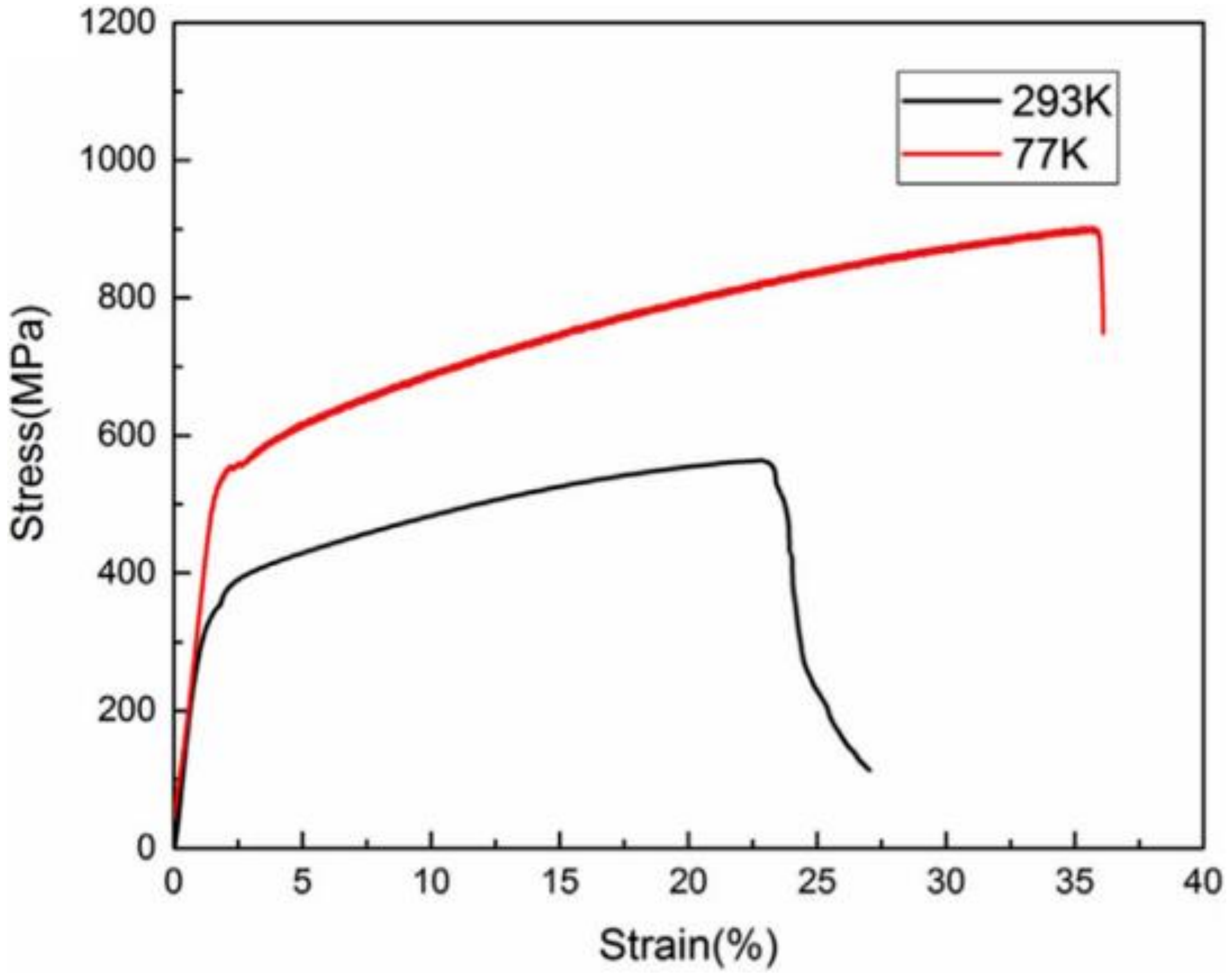

Fig. Tensile engineering stress–strain curve of the LPBFed CA, tested at 293 K and 77 K

Source: Chen et al. 2018 [https://doi.org/10.3390/e20120937]

Cantor alloy

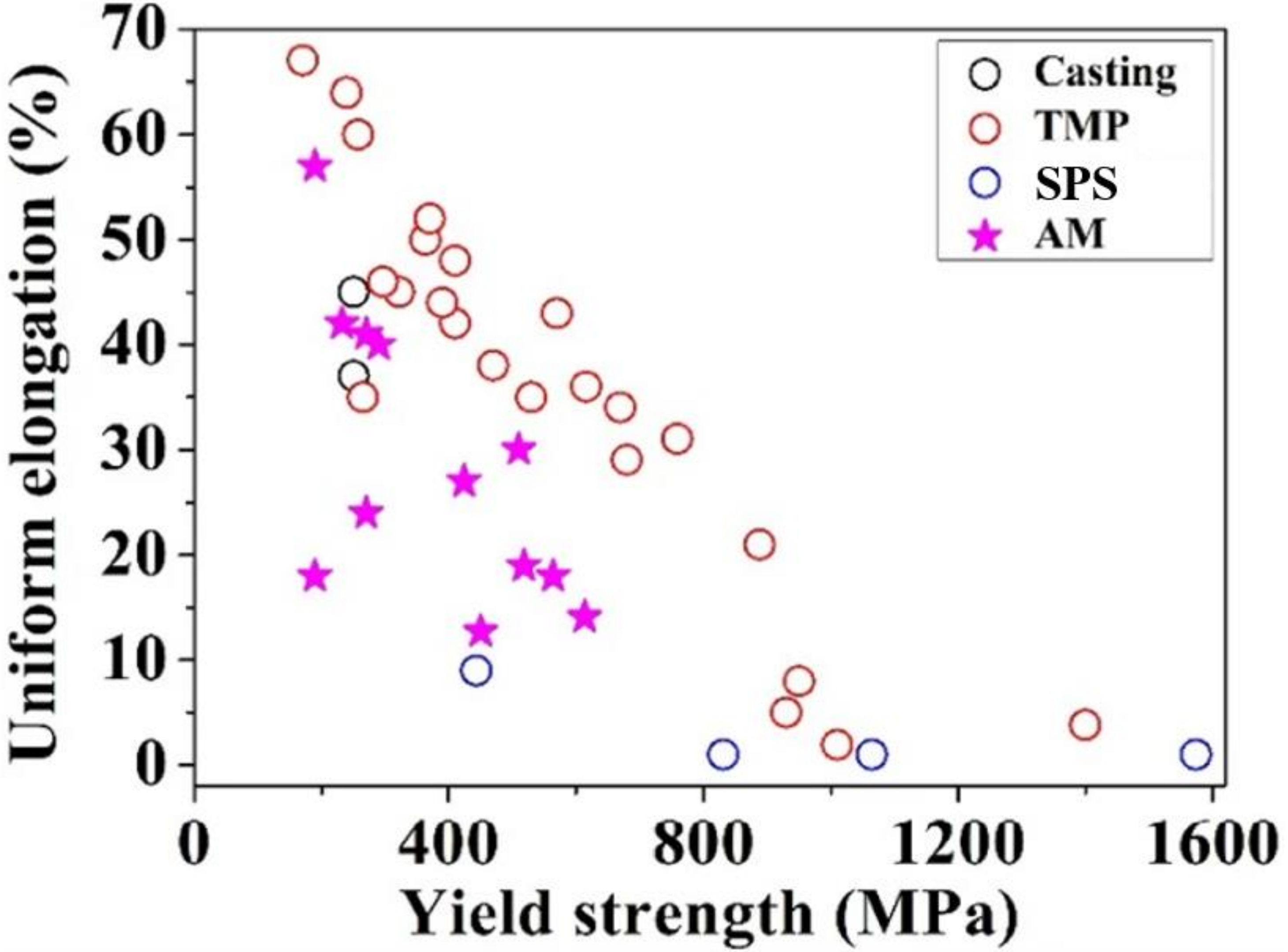

Fig. An overview of CA processed using various manufacturing techniques, including casting, thermo-mechanical processing (TMP), spark plasma sintering (SPS), and AM

Source: Guan et al. 2021 [https://doi.org/10.1007/s11669-021-00913-w]

Al-modified Cantor alloy

Fig. TEM micrographs of various AMed Al-modified Cas: (a)-(b) FCC precipitates in AlCoCrFeNi after ageing at 600°C for 168 h, (c)-(e) BCC (B2) precipitates (yellow circle) in the FCC matrix of AlCoCuFeNi after ageing at 1000°C for 10 h, and (f)-(g) L12 precipitates in $Al_{0.2}Co_{1.5}CrFeNi_{1.5}Ti_{0.3}$ after ageing at 750°C for 50 h

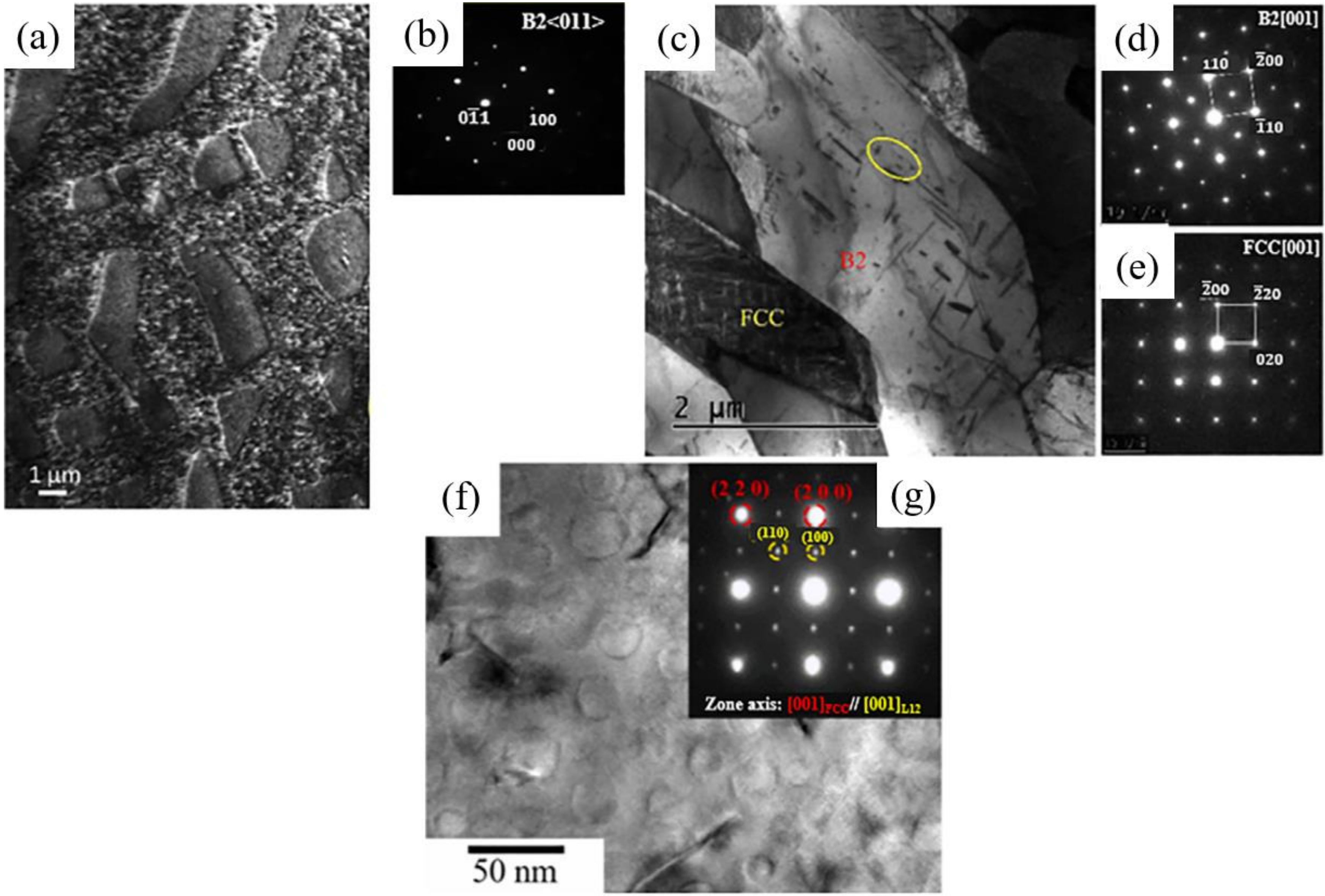

Source: [(a),(b)]Wang et al. 2017 [https://doi.org/10.1016/j.jallcom.2016.10.138]
[(c)-(e)]Zhang et al. 2019 [https://doi.org/10.1016/j.msea.2018.11.118]
[(f)]Lin et al. 2020 [https://doi.org/10.1016/j.addma.2020.101601]

Al-modified Cantor alloy

Fig. Comparison of the microstructure of the cast and LPBFed AlCoCrFeNi HEA: (a) EBSD IPF map of the LPBFed as-built and (b) cast specimens (Cracks are marked with black arrows in the LPBFed as-built sample. The black boxes in (a) and (b) are the regions that are used to extract the samples for compositional analysis), (c) Atom probe tomography of the LPBFed as-built and (d) cast counterpart, showing the 3D distribution of the atoms Al, Co, Cr, Fe, and Ni, (e) 1D element concentration profile along the build direction of the LPBFed as-built, and (f) the cast counterpart.

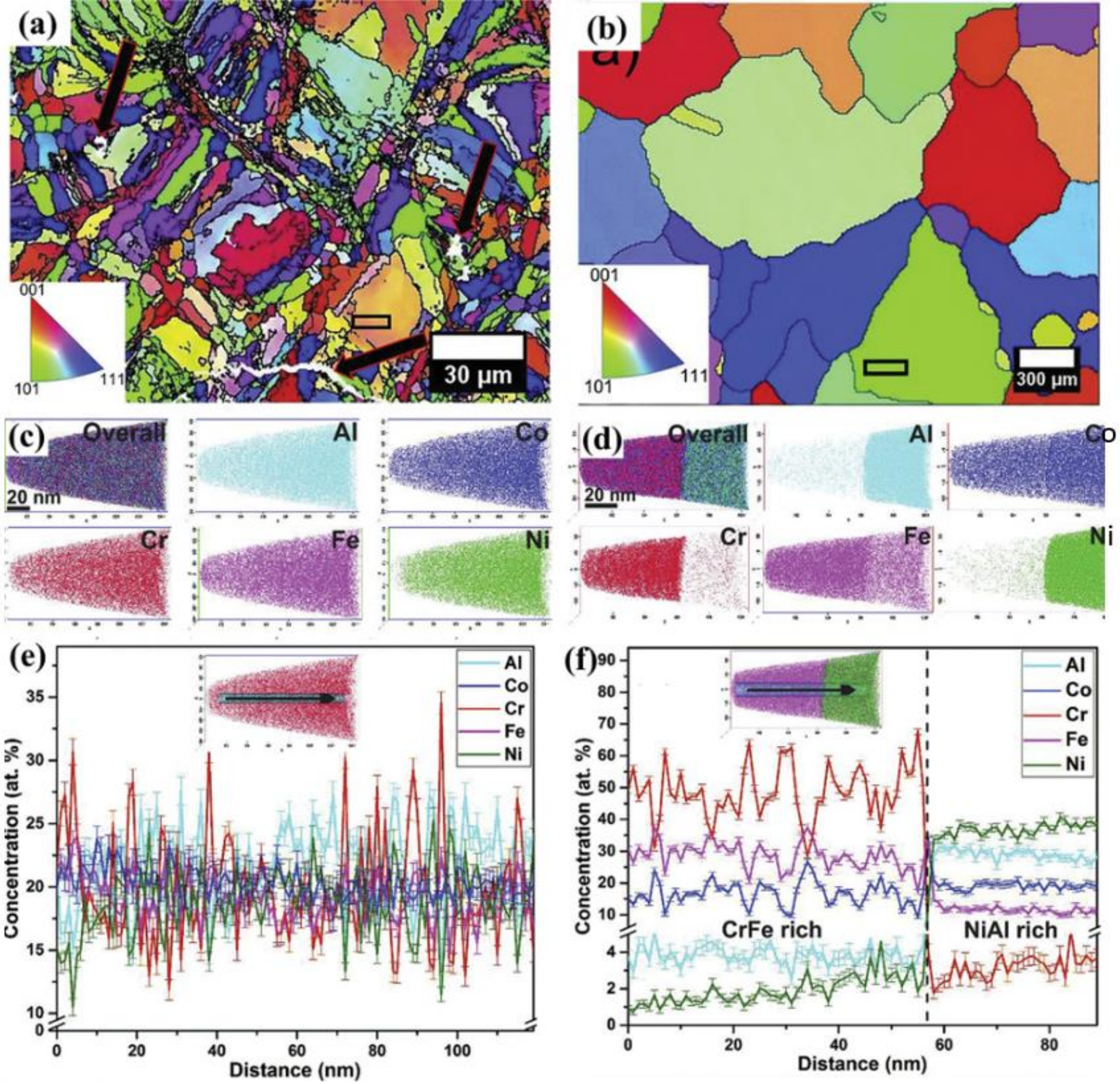

Source: Han et al. 2020 [https://doi.org/10.1002/adma.201903855]

Al-modified Cantor alloy

Fig. Schematic illustration of how the equiatomic AlCoCrFeNi HEA microstructure changes during EBM and casting

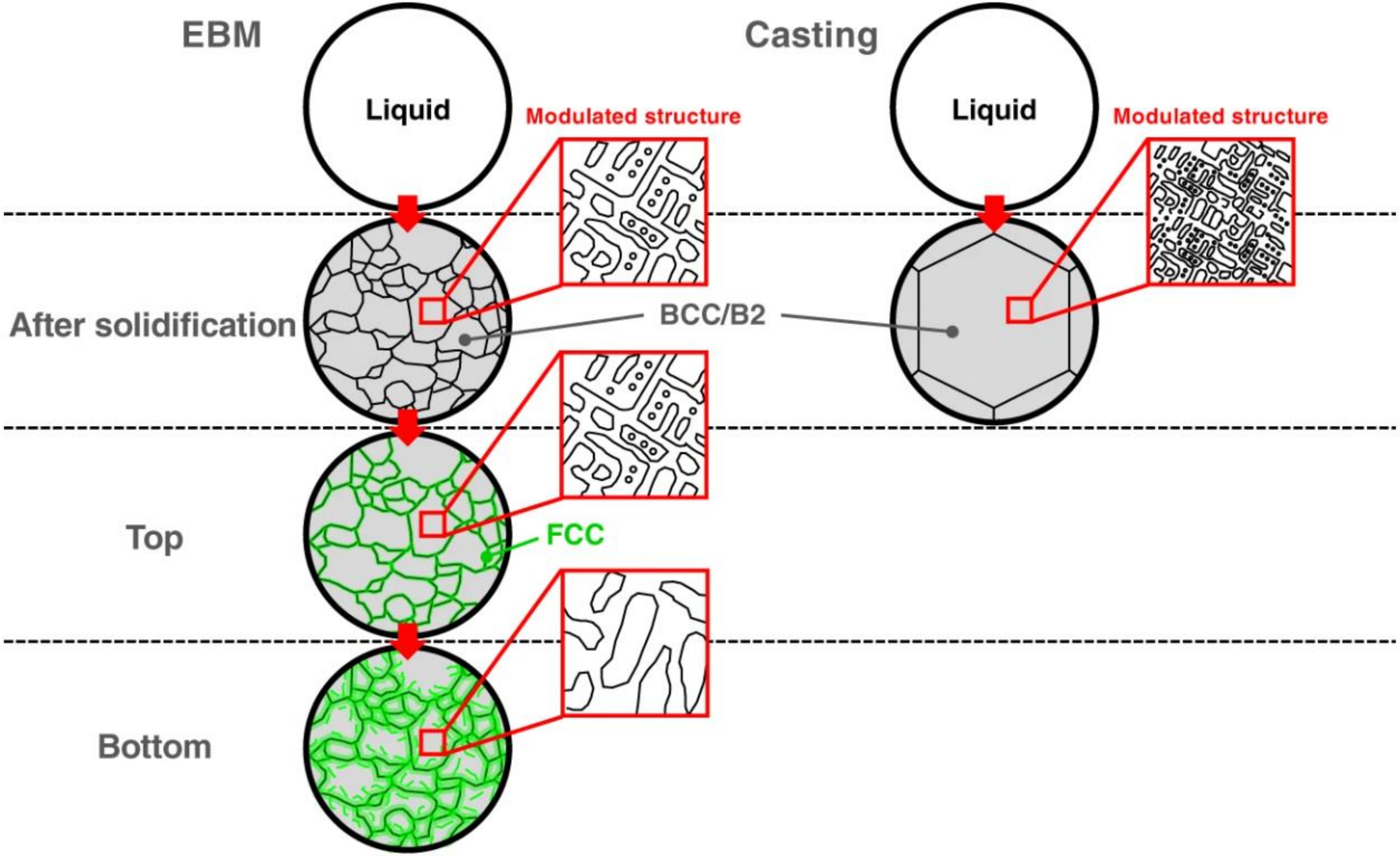

Source: Yamanaka et al. 2020 [https://doi.org/10.1038/s41529-020-00127-4]

Al-modified Cantor alloy

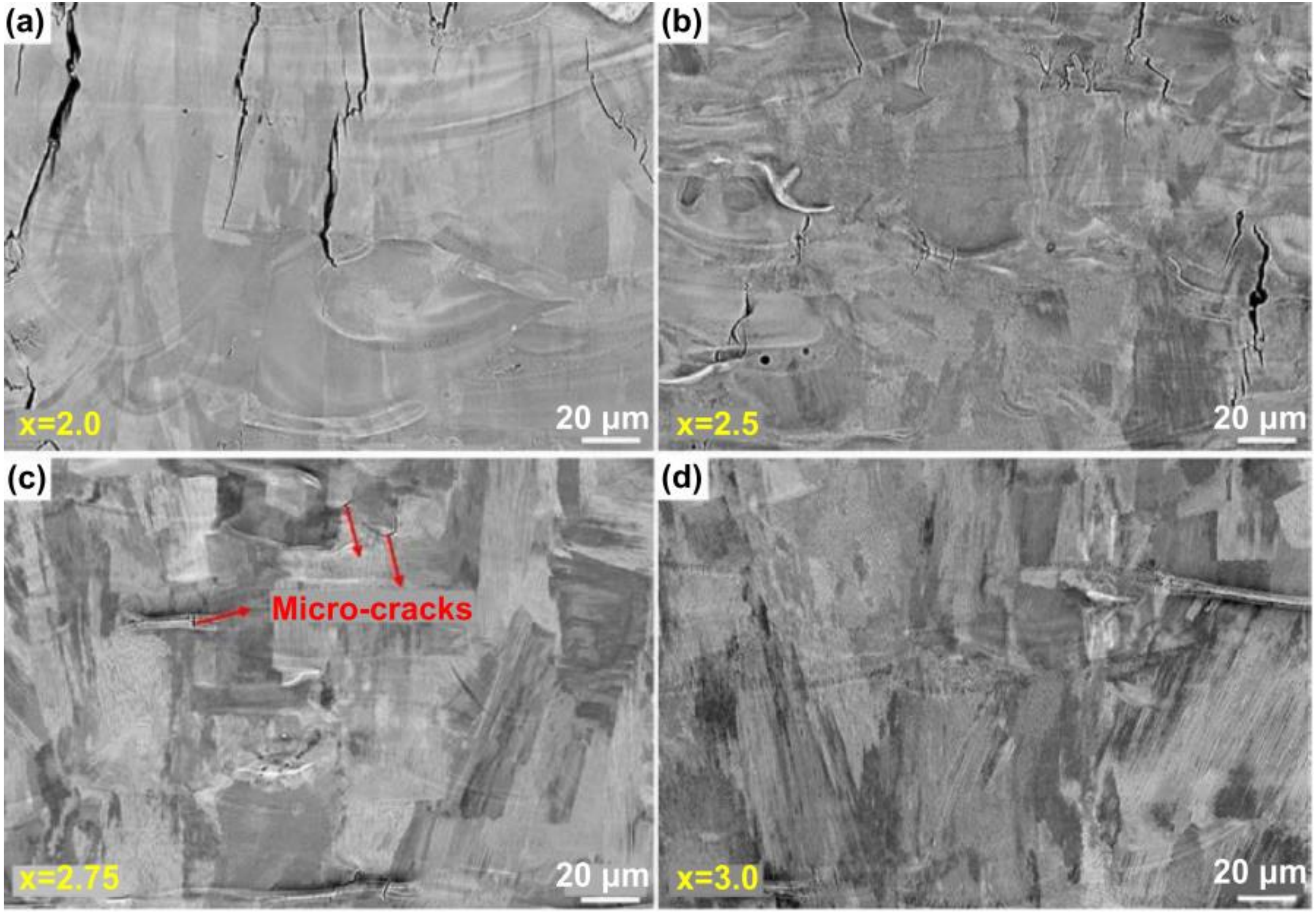

Fig. SEM micrographs of the LPBFed AlCrCuFeNix, showing crack mitigation by an increase in Ni content: (a) x = 2.0, (b) x = 2.5, (c) x = 2.75, and (d) x = 3.0

Source: Luo et al. 2020 [https://doi.org/10.1016/j.addma.2019.100925]

Al-modified Cantor alloy

Fig. (a) True tensile stress-strain curves of the as-cast and LMDed in various directions, as shown schematically (SD is the scan direction and DD is the deposition direction) of an $AlCoCrFeNi_{2.1}$ HEA, (b) and (c) SEM micrographs showing the fracture surface of the LMDed sample deformed in the scan direction

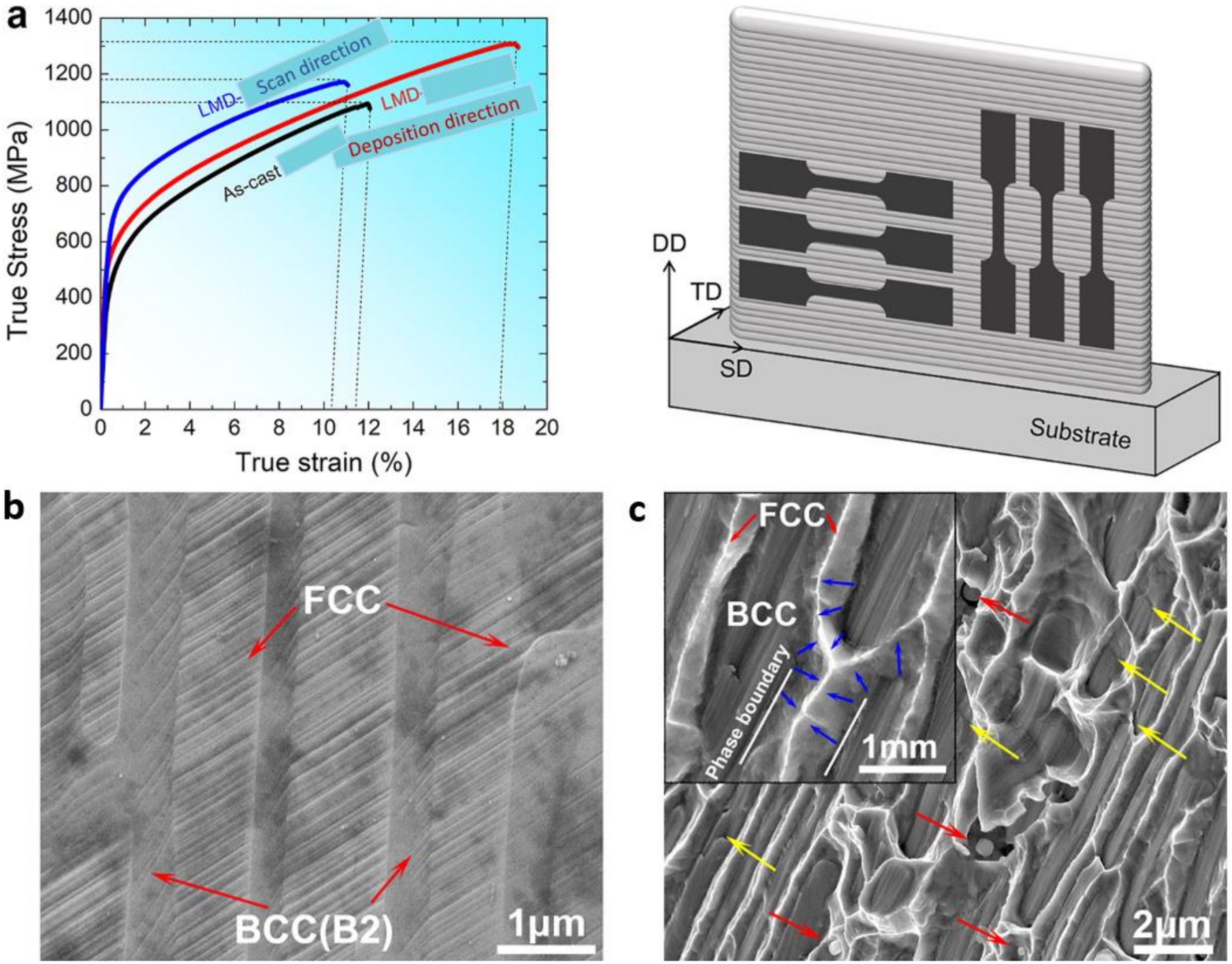

Source: Huang et al. 2022 [https://doi.org/10.1016/j.msea.2021.142327]

Other variations of Cantoralloy

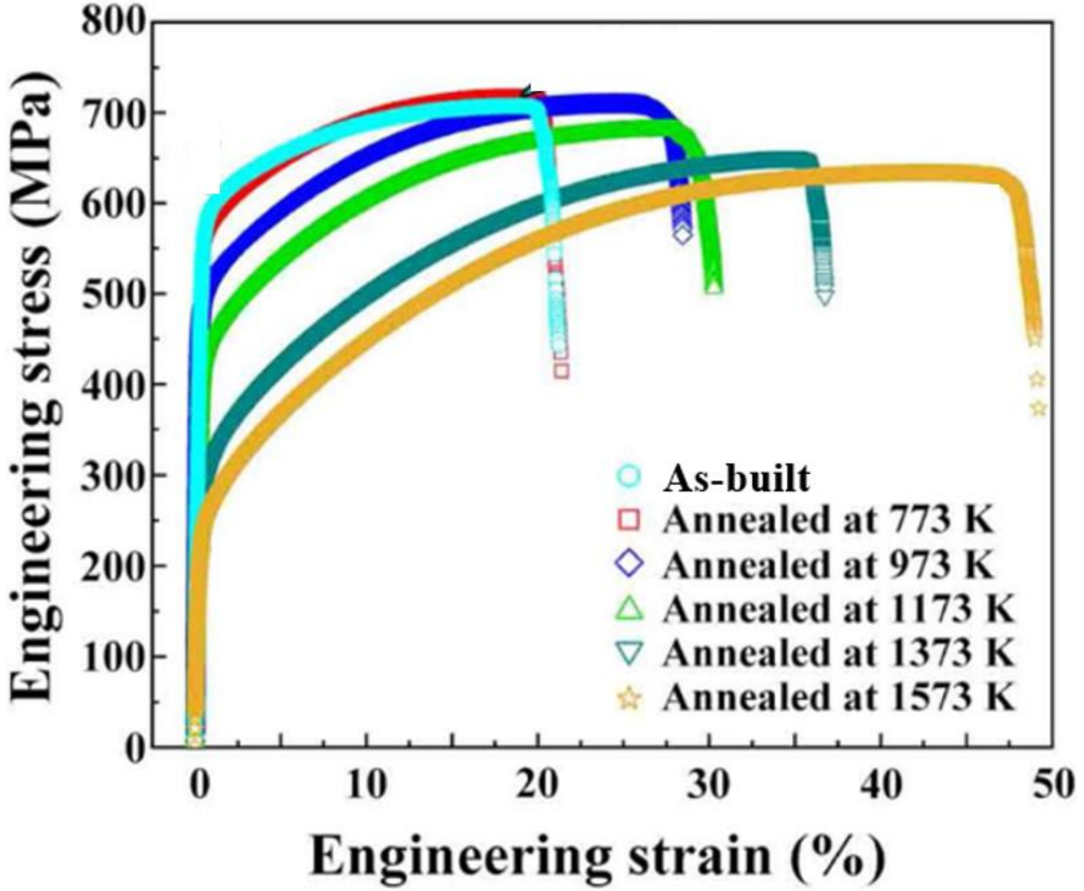

Fig. Engineering stress-strain curve of LPBFed FeCoCrNi HEA in the as-built state and annealed at various temperatures after printing

Source: Lin et al. 2020 [https://doi.org/10.1016/j.addma.2020.101058]

Other variations of Cantoralloy

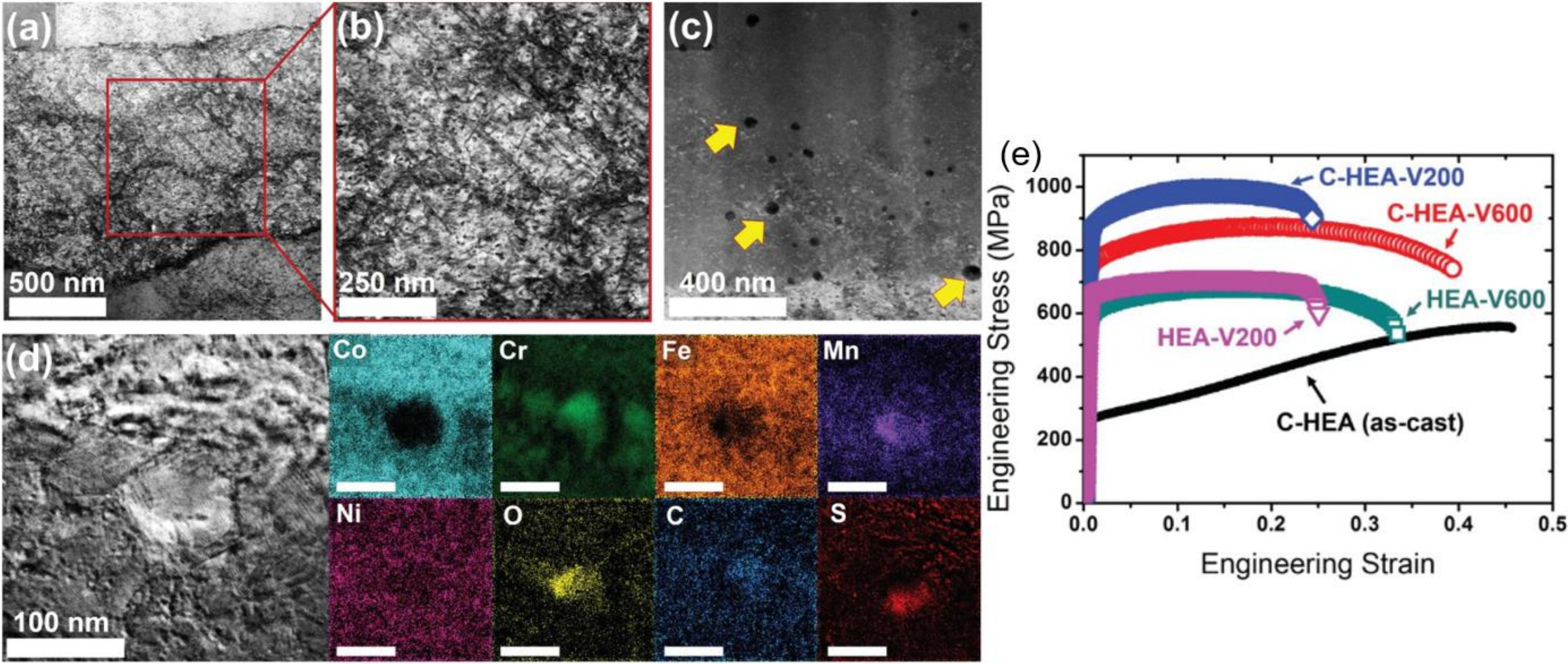

Fig. TEM micrographs of: (a) cellular structures, (b) magnified image of the red rectangle in (a) for C-HEA, (c) STEM micrographs indicating the presence of nanoprecipitates, (d) EDS mapping micrographs of both substitutional (Co, Cr, Fe, Mn, and Ni) and interstitial (O, C, and S) elements for the nanoprecipitates are shown in the TEM micrographs of the LPBFed C-HEA, and (e) Tensile properties of the C-HEAs and CA LPBFed with various processing parameters, as well as in the as-cast condition

Source: Park et al. 2020 [https://doi.org/10.1080/21663831.2019.1638844]

Other variations of Cantoralloy

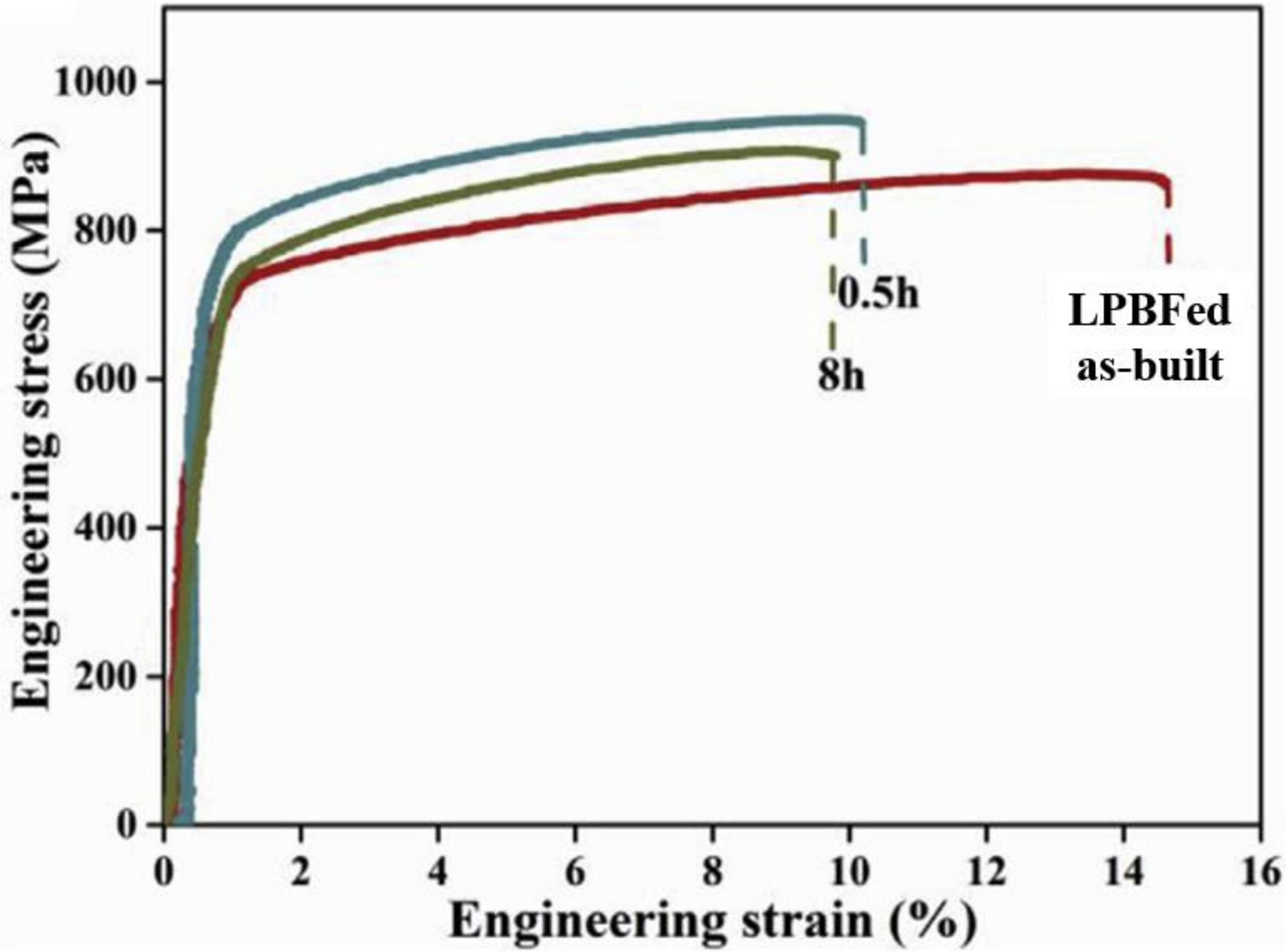

Fig. Engineering stress-strain curves of the LPBFed as-built and annealed (at 1073 K for 0.5 h and 8 h) samples of eCoCrNi$C_{0.05}$ HEA

Source: Zhou et al. 2019 [https://doi.org/10.1016/j.intermet.2018.12.001]

Other variations of Cantoralloy

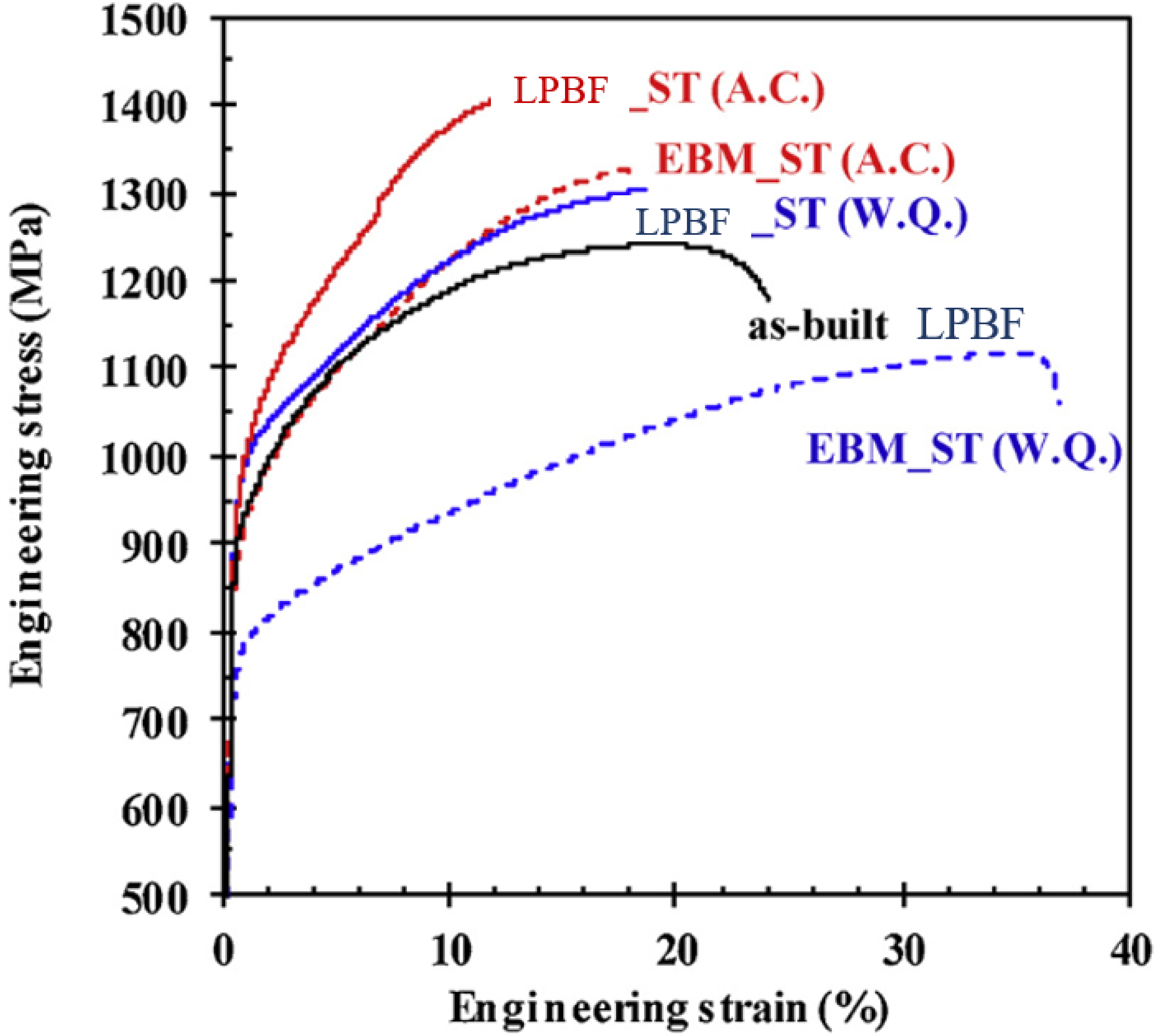

Fig. Engineering stress-strain curves of the LPBFed as-built and heat treated at 1393 K for 3 hours followed by air cooling (ST A.C.) or water quenching (ST W.Q.), as well as EBMed and heat treated (similar heat treatment scheme with LPBFed samples) samples of $CoCrFeNiTi_7Mo_3$ HEA

Source: Fujieda et al. 2019 [https://doi.org/10.1016/j.addma.2018.10.023]

Other variations of Cantoralloy

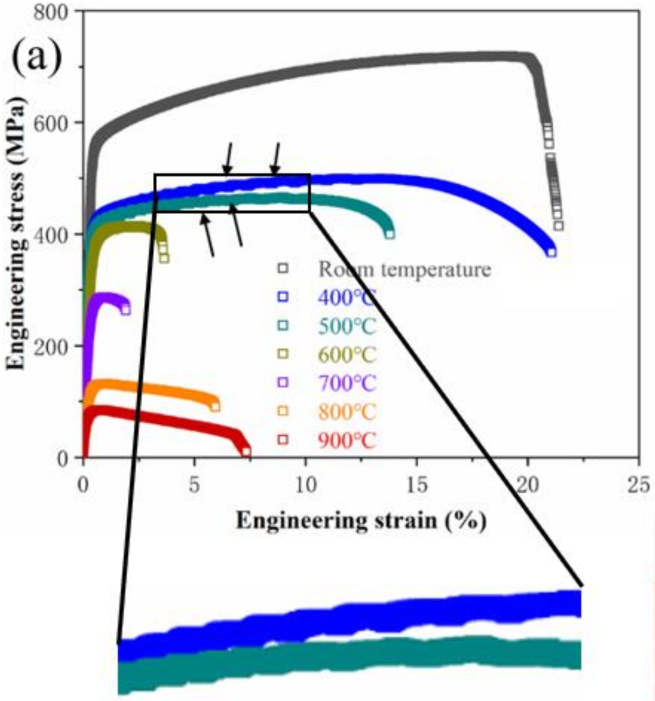

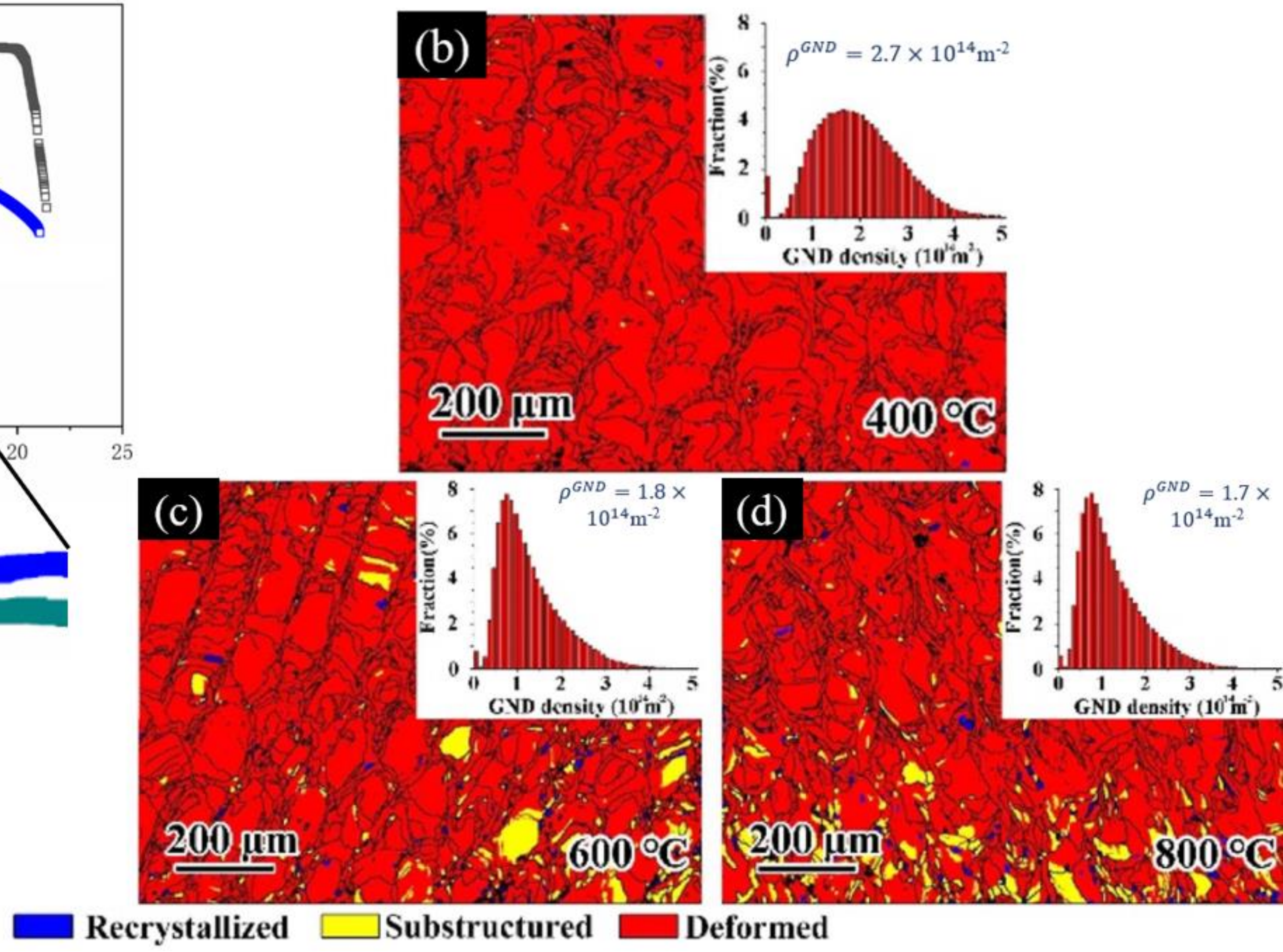

Fig. (a) Stress-strain curves of LPBFed FeCoCrNi HEA deformed at various temperatures with a strain rate of 5×10^{-3} min^{-1}. Serrations during deformation at 400 and 500°C are indicated with arrows and shown in the magnified inset, Recrystallization maps indicating recrystallized (blue), substructured (partially recrystallized, yellow), and deformed (red) grains in the deformed samples at (b) 400°C, (c) 600°C, and (d) 800°C (GND density (ρGND) is also shown in the insets)

Source: Lin et al. 2022 [https://doi.org/10.1016/j.msea.2021.142354]

Refractory high-entropy alloys

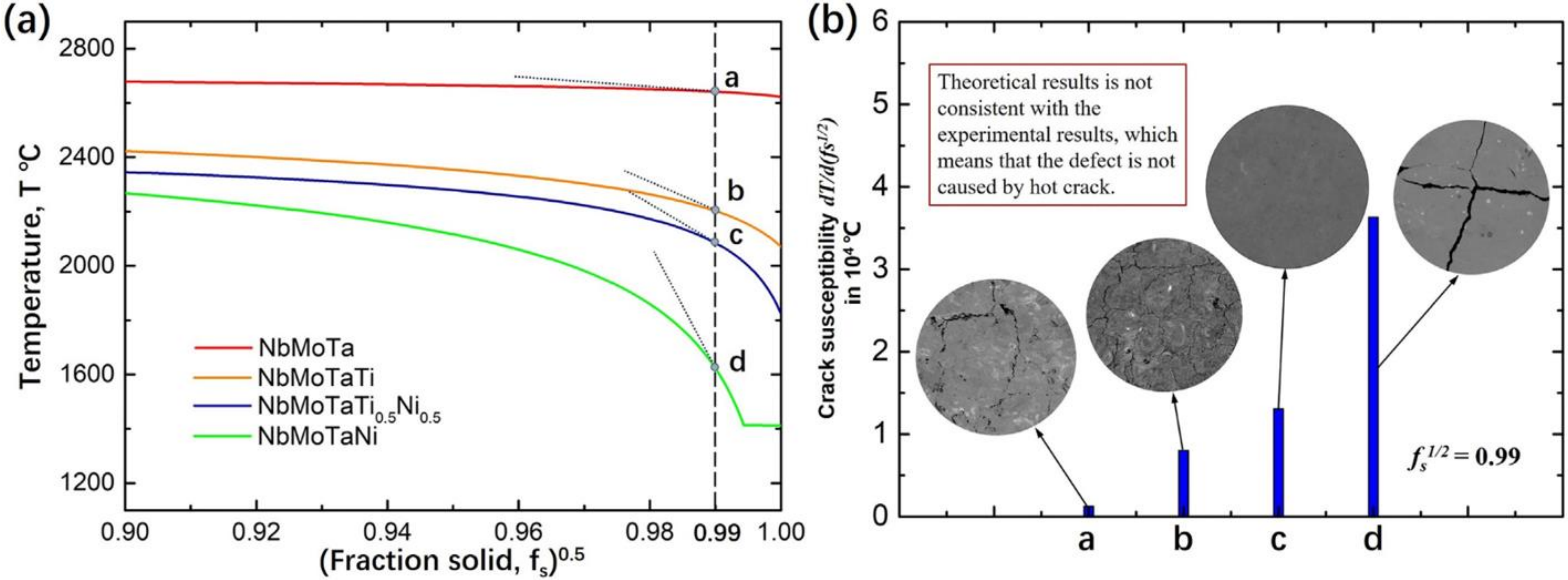

Fig. (a) Solidification path calculated by Thermo-Calc and (b) crack susceptibility index of NbMoTaX alloys

Zhang et al. 2021 [https://doi.org/10.1016/j.matdes.2021.109462]

Refractory high-entropy alloys

Fig. (a) TEM micrograph of the interstitial phase in NbMoTaTi alloy, (b) the fracture of GB phase in NbMoTaTi alloy under stress F, and (c) stacking faults in GB phase of $NbMoTaTi_{0.5}Ni_{0.5}$

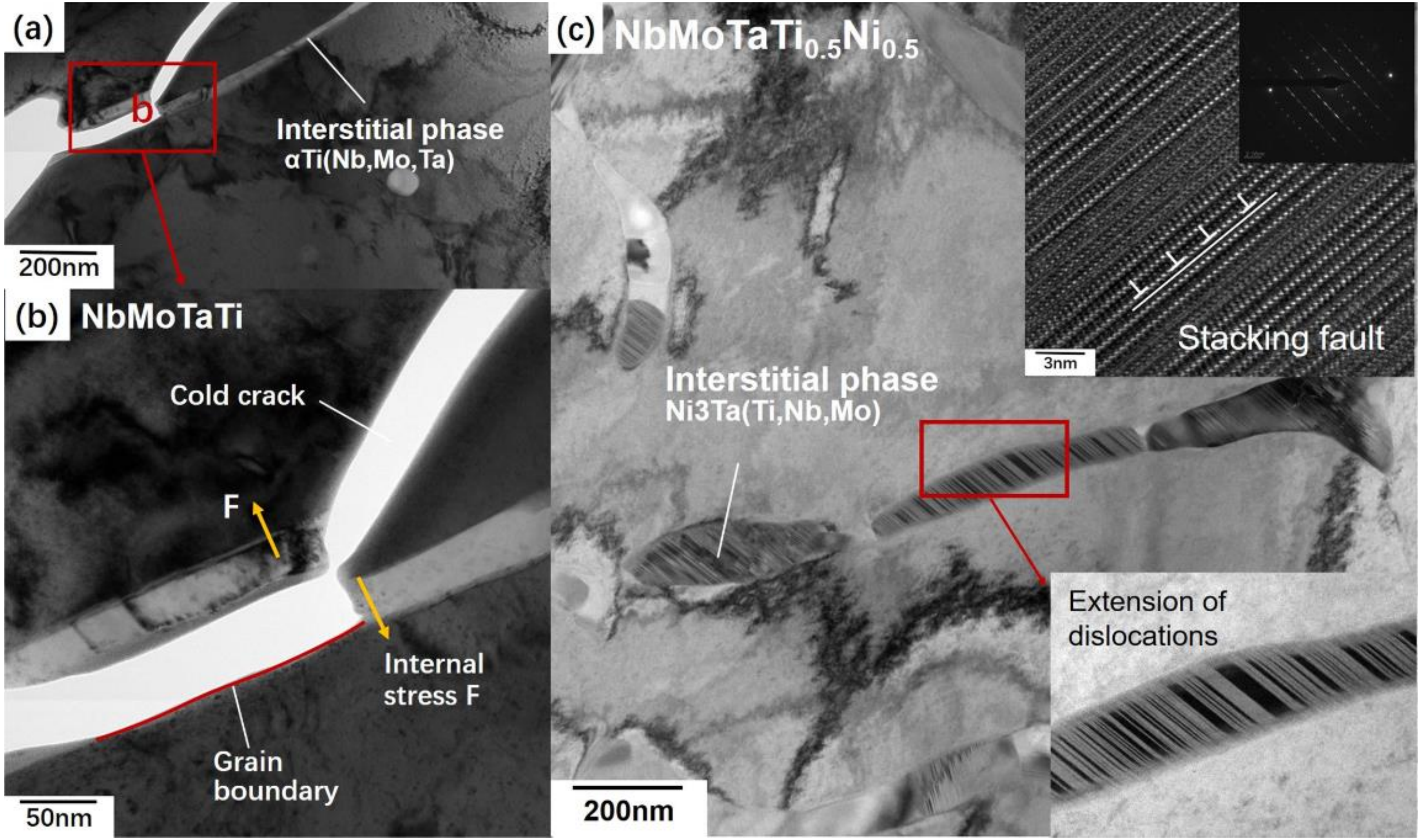

Zhang et al. 2021 [https://doi.org/10.1016/j.matdes.2021.109462]

Refractory high-entropy alloys

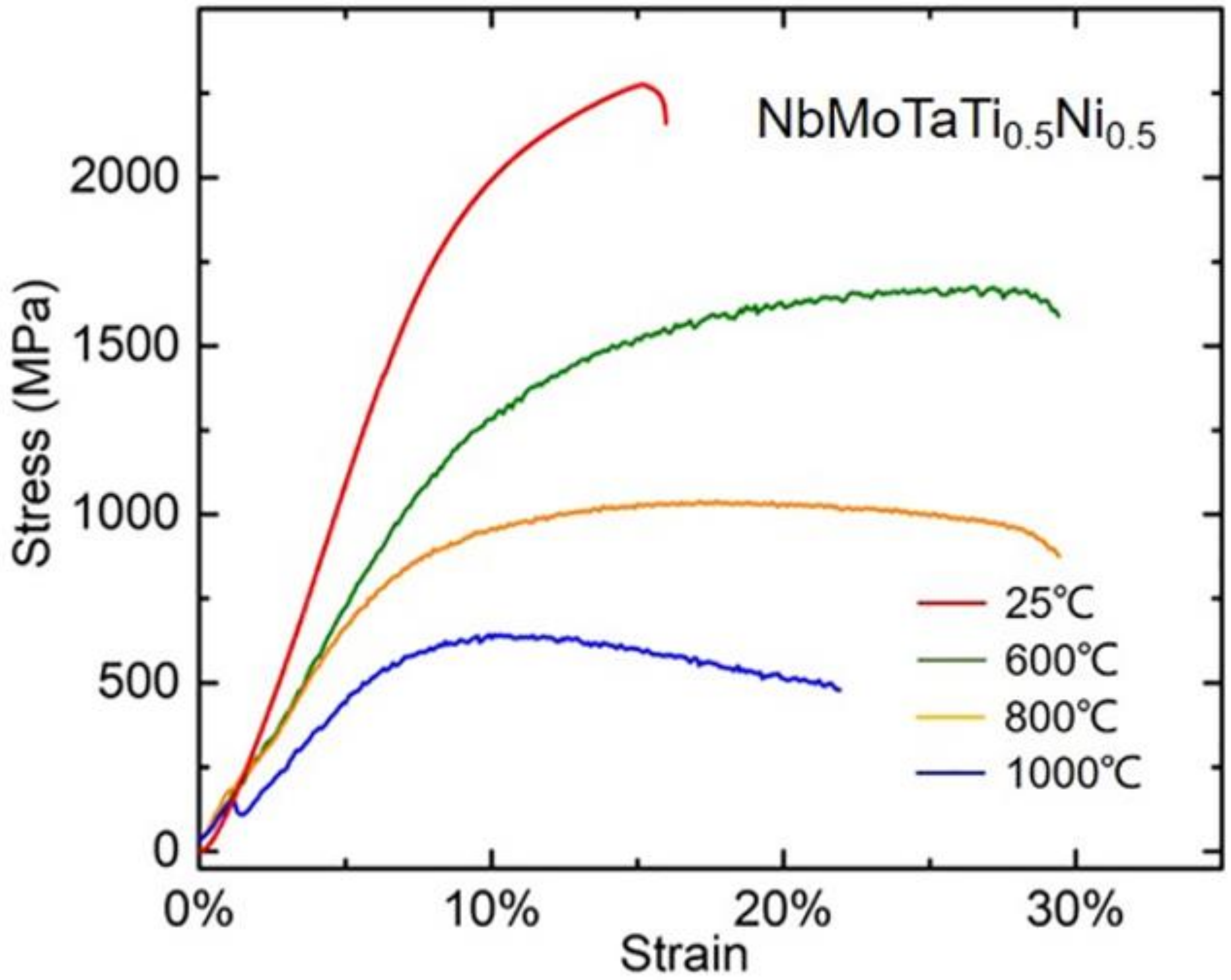

Fig. Compressive stress-strain curves of LPBFed $NbMoTaTi_{0.5}Ni_{0.5}$ HEA at room and elevated temperatures

Zhang et al. 2021 [https://doi.org/10.1016/j.matdes.2021.109462]

Refractory high-entropy alloys

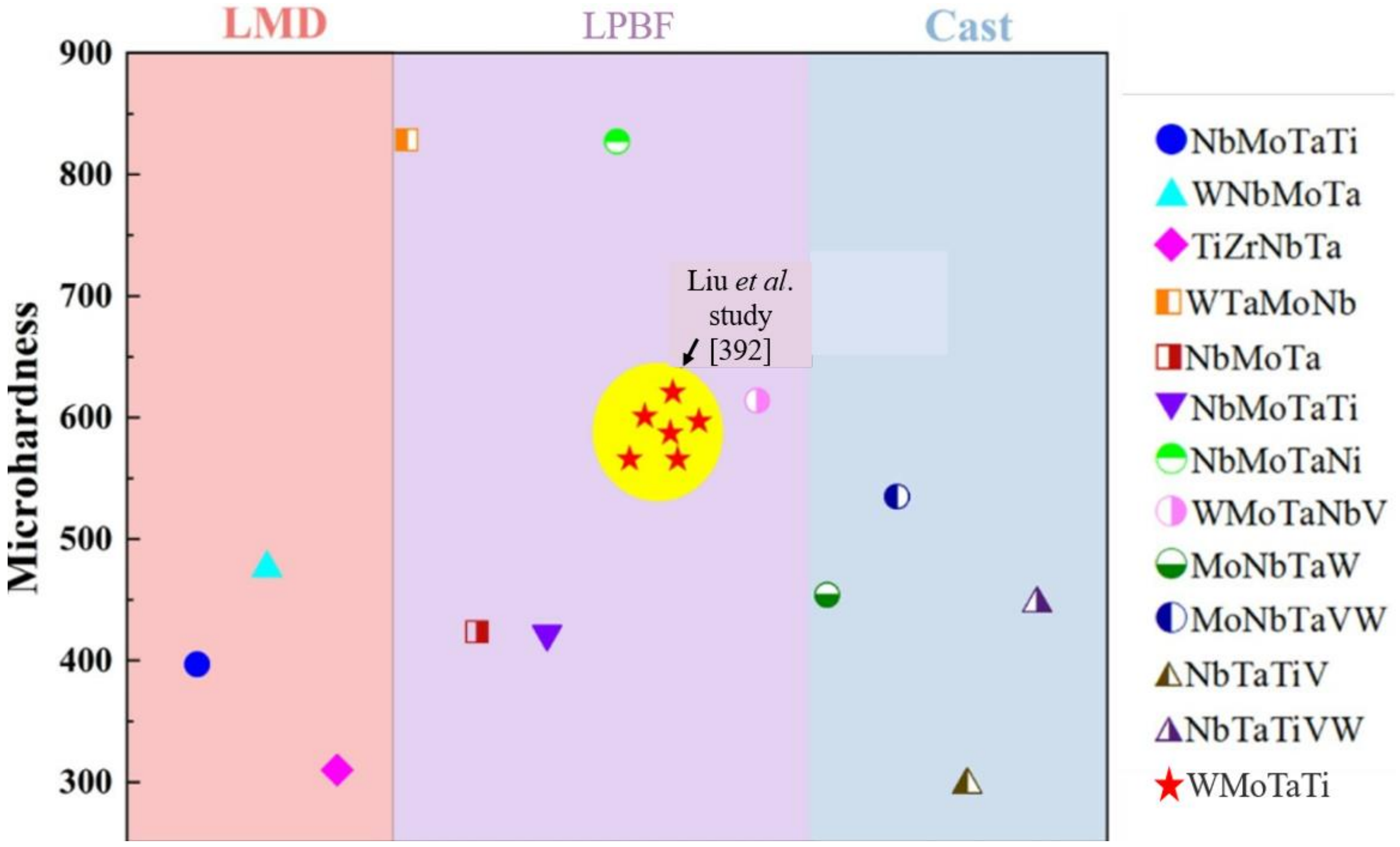

Fig. Summary of microhardness of the commonly reported RHEAs produced by LMD, LPBF, and casting

Source: Liu et al. 2022 [https://doi.org/10.1080/00325899.2022.2031718]

Summary

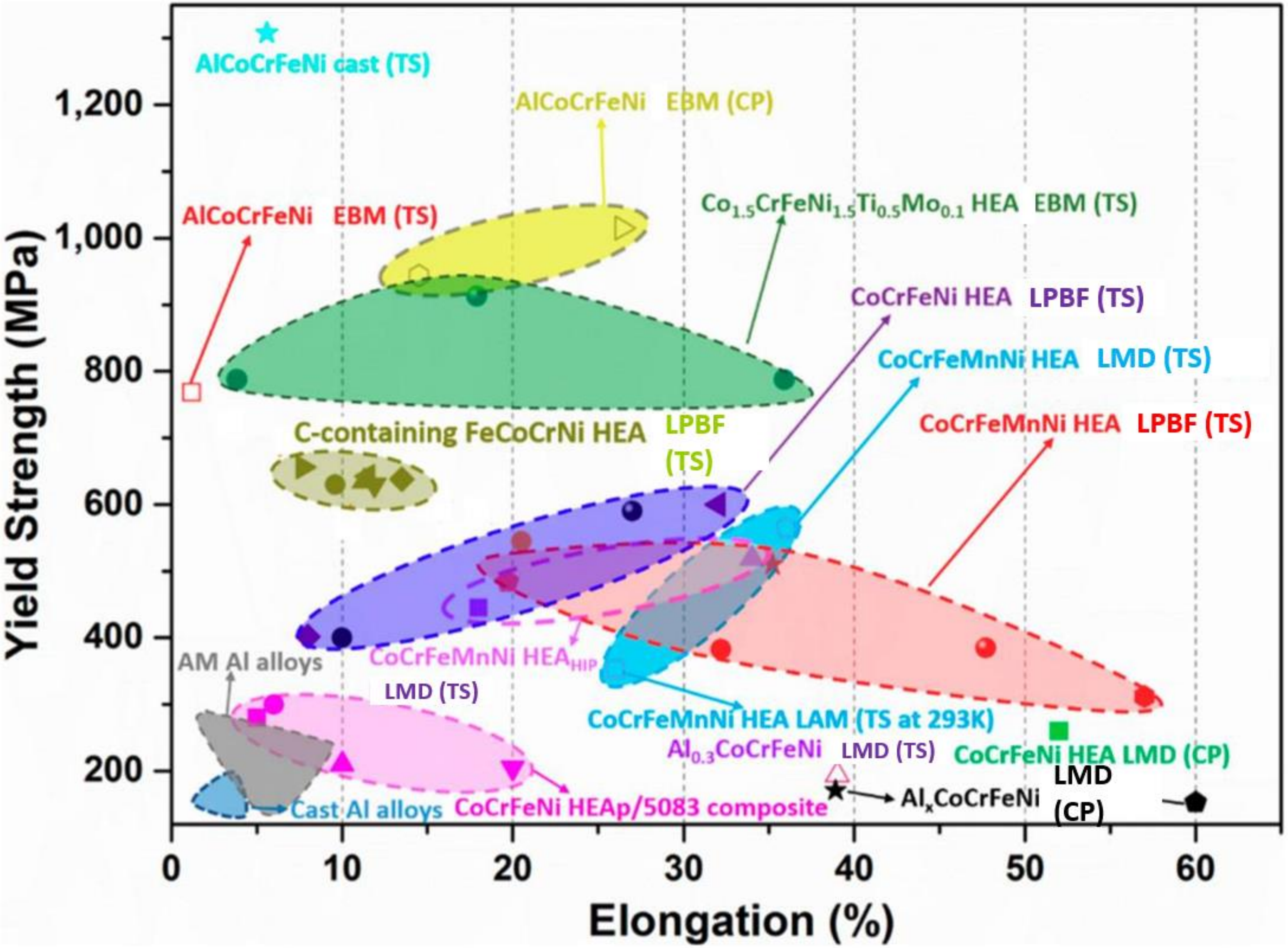

Fig. Yield strength elongation of various HEAs and Al alloys produced via various AM techniques and casting

Source: Chen et al. 2018 [https://doi.org/10.3390/e20120937]